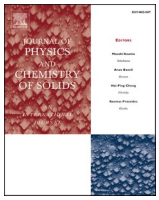
Journal of Physics and Chemistry of Solids 222 (2027) 114303



Contents lists available at ScienceDirect

Journal of Physics and Chemistry of Solids

journal homepage: www.elsevier.com/locate/jpcs



Heterointerface engineering in $CaFe_2O_4/MgFe_2O_4$ composite fibers for enhanced magnetic performance

Zhibin Ling [a,1], Feiyu Diao [a,1], Fei Xie [a], Rongsheng Cai [b], Xuyan Xue [a,*], Yiqian Wang [a,**]

[a] College of Physics, Qingdao University, No. 308 Ningxia Road, Qingdao, 266071, PR China
[b] State Key Laboratory of Solid Lubrication, Lanzhou Institute of Chemical Physics, Chinese Academy of Sciences, Lanzhou, 730000, PR China

A B S T R A C T

Alkaline-earth metal-based spinel ferrites, in particular $CaFe_2O_4$ and $MgFe_2O_4$, are promising soft magnetic materials for next-generation magnetic sensing and biomedical applications, but their performance is often limited by inherently weak magnetization. In this work, $CaFe_2O_4/MgFe_2O_4$ composite fibers are fabricated by electrospinning and high-temperature annealing. Structural and microstructural characterization confirms formation of abundant coherent heterointerfaces between orthorhombic $CaFe_2O_4$ and cubic $MgFe_2O_4$ in the composite fibers, with well-defined crystallographic orientation relationships. These heterointerfaces play a pivotal role in boosting the magnetic response of the composite fibers. The $CaFe_2O_4/MgFe_2O_4$ composite fibers exhibit significantly enhanced saturation magnetization of 23.60 emu/g, which is approximately 120 times that of pure $CaFe_2O_4$ (0.19 emu/g) and 3.7 times that of pure $MgFe_2O_4$ (6.46 emu/g). First-principles calculation is carried out to clarify the underlying mechanism of this enhancement, which shows that interfacial coupling modifies the electronic structure of Fe to reduce spin-down density, thereby increasing the net magnetic moment. This study demonstrates that heterointerface engineering provides an effective route for developing high-performance soft magnetic ferrites.

1. Introduction

The rapid development of modern telecommunications and magnetic sensing with high precision has led to an increasing demand for soft magnetic materials with efficient high-frequency performance [1–3]. Among various candidates, alkaline-earth metal-based spinel ferrites, particularly $CaFe_2O_4$ and $MgFe_2O_4$, have garnered widespread interest owing to their affordability, exceptional chemical robustness, and environmental friendliness [4,5]. Unlike $SrFe_2O_4$ and $BaFe_2O_4$, which are archetypal hard magnets used in permanent magnets and recording media [6–8], $CaFe_2O_4$ and $MgFe_2O_4$ exhibit soft magnetic behavior that is more suitable for low-loss, high-frequency operations [9–12]. Such attributes render these compounds highly suitable for diverse technological implementations, from traditional inductors and transformers to advanced magnetic sensors and biomedical devices [13–18]. However, the inherently weak saturation magnetization (M_s) of $CaFe_2O_4$ and $MgFe_2O_4$ remains a major bottleneck, hindering their practical integration into next-generation high-performance magnetic technologies [19–21].

Considerable research efforts, including the exploration of morphology control, elemental doping, and heterointerface engineering, have been dedicated to optimizing the magnetic properties of $CaFe_2O_4$ and $MgFe_2O_4$. Morphology control has primarily focused on controllable preparation of nanoparticles, whose magnetic performance is tuned *via* particle size and crystallinity. For instance, Kameli et al. [22] reported a size-dependent increase in the M_s of $MgFe_2O_4$ nanoparticles, while Das et al. [20] demonstrated that heat treatment at different temperatures can effectively influence the microstructure and M_s of $CaFe_2O_4$ nanoparticles. Elemental doping has also been proven to be an effective strategy, *i.e.*, Cu doping for enhanced magnetization of $MgFe_2O_4$ [23] and Ni doping for improved M_s and coercivity (H_c) of $CaFe_2O_4$ [24]. For the heterointerface engineering strategy, although it has been applied to improve photocatalytic and gas-sensing properties [25–30], its application for enhancing magnetic performance remains underexplored. In addition, one-dimensional (1D) nanostructures often exhibit better magnetic properties than zero-dimensional particles due to enhanced shape anisotropy and constrained domain wall motion [31–33]. Despite the single advantage of 1D architectures and interfacial engineering, their synergistic integration has not been rigorously explored. Moreover, the fundamental mechanism, by which interfacial coupling between different phases (*i.e.*, orthorhombic $CaFe_2O_4$ and cubic $MgFe_2O_4$) influences their electronic structure and net magnetic

* Corresponding author.
** Corresponding author.
E-mail addresses: xuexy@qdu.edu.cn (X. Xue), yqwang@qdu.edu.cn (Y. Wang).
[1] These authors contributed to this work equally.

https://doi.org/10.1016/j.jpcs.2026.114303
Received 20 September 2026; Received in revised form 3 November 2026; Accepted 15 November 2026
Available online 16 November 2026
0022-3697/© 2026 Elsevier Ltd. All rights are reserved, including those for text and data mining, AI training, and similar technologies.

moment, is still lacking.

In this work, $CaFe_2O_4/MgFe_2O_4$ composite fibers with coherent heterointerfaces were fabricated using electrospinning combined with subsequent annealing in air at high temperatures. Magnetic hysteresis loop analysis showed that the composite fibers possessed significantly enhanced saturation magnetization compared to single-phase fibers. Complementary first-principles density functional theory (DFT) calculations were carried out to uncover the microscopic origin of magnetic enhancement. These findings not only demonstrate an effective approach for boosting the magnetic properties of alkaline-earth metal ferrites, but also offer deeper mechanistic understanding of the effect of interfacial coupling on the modulation of local electronic configurations.

2. Experimental

2.1. Materials

Calcium acetylacetonate [Ca $(acac)_2$, ≥98%], magnesium acetylacetonate [Mg $(acac)_2$, ≥98%], iron acetylacetonate [Fe $(acac)_3$, ≥98%] and polyvinylpyrrolidone (PVP, molecular weight: 1,300,000), were purchased from Sinopharm Chemical Reagent Company Limited. All chemicals were utilized as supplied without further treatment.

2.2. Preparation of $CaFe_2O_4$, $MgFe_2O_4$, and $CaFe_2O_4/MgFe_2O_4$ fibers

Electrospinning was employed to produce $CaFe_2O_4$, $MgFe_2O_4$, and $CaFe_2O_4/MgFe_2O_4$ fibers. Precursor salts were first weighed according to the stoichiometric proportions summarized in Table 1 and transferred into a glass vial. 0.66 g of PVP was added into this mixture, together with ethanol (3 mL) and acetic acid (3 mL) in sequence. The resulting suspension was magnetically stirred for 6 h until a transparent and viscous solution formed.

For fiber fabrication, a portion of this solution (3-5 mL) was then loaded into a plastic syringe and electrospun under the following parameters, adapted from previous reports [34–36]: feeding rate = 0.5 mL/h, working voltage = 16 kV, collection distance = 15 cm, and rotating speed of the steel plate collector = 500 rpm (the collector was covered with oil paper). The spinning chamber was maintained at 25 °C with a relative humidity of ~45%. Upon completion of electrospinning, the as-spun fibrous membranes were peeled off from the collector, pre-dried at 60 °C for 2 h to eliminate residual solvent, and followed by a calcination process at 900 °C for 12 h in air, with a heating ramp of 5 °C/min. The resulting products were designated as CF-12, MF-12, and CMF-114, corresponding to initial Ca:Fe, Mg:Fe, and Ca:Mg:Fe molar ratios of 1:2, 1:2, and 1:1:4, respectively.

2.3. Characterization

Crystallographic phases of the as-prepared fibers were probed *via* X-ray diffraction (XRD, Bruker D8 Advance) employing Cu-K_α radiation (λ = 1.5406 Å). Morphological inspection was performed *via* field-emission SEM (FE-SEM, Sigma 500) at an accelerating voltage of 15 kV. Further microstructural insights, including bright-field (BF), high-resolution transmission electron microscopy (HRTEM) imaging, and selected-area electron diffraction (SAED) patterns, were obtained on a JEOL JEM2100F microscope at 200 kV. The surface elemental valence states were analyzed by X-ray photoelectron spectroscopy (XPS) spectra (Thermo Scientific K-Alpha$^+$) with an Al K_α X-ray source. Energy-dispersive X-ray spectroscopy (EDS, Oxford INCAx-sight 6427) was utilized to acquire elemental maps of the fiber specimens, and high-angle annular dark-field (HAADF) imaging was realized on a probe-corrected Thermo Scientific Spectra 300 (S)TEM operated at 300 kV. Finally, the room-temperature magnetic response was measured using a vibrating sample magnetometer (VSM) within a physical properties measurement system (PPMS, Quantum Design).

Table 1
Precursor salt ratios for different products.

Precursor salts				Product name
Ca $(acac)_2$(g)	Mg $(acac)_2$(g)	Fe $(acac)_3$ (g)	Molar ratio	
0.24	/	0.70	1:2	CF-12
/	0.22	0.70	1:2	MF-12
0.12	0.11	0.70	1:1:4	CMF-114

2.4. Computational methodology

The first-principles calculations were carried out using the Vienna *ab initio* Simulation Package (VASP) [37] code based on DFT. The generalized gradient approximation (GGA) in the PBE formulation was implemented to describe exchange-correlation interactions, alongside the projector augmented wave (PAW) pseudopotential for ion-core treatment [38]. A plane-wave cutoff energy of 520 eV and a *k*-point spacing of $2\pi\times0.025$ Å^{-1} were employed for the calculations. For structural relaxation, the energy and force convergence thresholds were set to be 10^{-6} eV and 0.01 eV/Å. The spin-polarized partial densities of states (PDOS) and magnetic moments were computed with collinear magnetism.

3. Results and discussion

3.1. Morphology and crystal structure of as-prepared products

The crystal structure of the as-synthesized products was examined by XRD (Fig. S1). All three samples exhibit well-defined diffraction peaks indicative of high crystallinity, with no detectable impurity phases. The CF-12 sample displays a pure orthorhombic $CaFe_2O_4$ (JCPDS No.: 72-1199, a = 9.230 Å, b = 10.705 Å, c = 3.024 Å), while the MF-12 sample is identified as single-phase cubic $MgFe_2O_4$ (JCPDS No.: 88-1935, a = 8.380 Å). For the CMF-114 sample, the diffraction pattern contains the characteristic reflections of both $CaFe_2O_4$ and $MgFe_2O_4$, confirming the formation of a biphasic composite. Quantitative analysis of the XRD pattern indicates that the molar ratio of $CaFe_2O_4$ and $MgFe_2O_4$ is close to 1:1.05 in the composite, consistent with the initial Ca:Mg molar ratio used in the raw materials.

SEM was employed to probe the morphological features of the three products. As presented in Fig. 1, all three samples exhibit well-defined fibrous morphologies, with differences in fiber diameter and surface features. Low-magnification image in Fig. 1a reveals that the $CaFe_2O_4$ fibers possess relatively rough surfaces. The high-magnification image in Fig. 1b demonstrates that the $CaFe_2O_4$ fibers are composed of uniformly-sized particles that are tightly bound together, resulting in a relatively dense fibrous architecture. Statistical size analysis from Fig. 1c indicates that the $CaFe_2O_4$ fibers have diameters predominantly in the range of 200-350 nm. In contrast, the $MgFe_2O_4$ fibers are composed of densely packed fine grains, as presented in Fig. 1d and e. These fibers have an average diameter of ~200 nm, ranging from 150 to 300 nm (Fig. 1f). The small grain size and numerous interparticle voids give rise to a porous surface with a relatively uniform pore distribution. Compared with the $CaFe_2O_4$ fibers, the $MgFe_2O_4$ fibers consist of smaller grains, which might contribute to the magnetic performance of the ferrites.

The $CaFe_2O_4/MgFe_2O_4$ composite fibers are composed of numerous small particles, as illustrated in the low- and high-magnification SEM images in Fig. 1g and h, respectively. In contrast to the single-phase fibers, the composite fibers exhibit a slightly larger diameter, with most fibers falling in the range of 300-400 nm, as determined from the statistical analysis in Fig. 1i. High-magnification SEM image in Fig. 1h reveals that the surface roughness and granular microstructure of the composite fibers is analogous to that of the single-phase $CaFe_2O_4$ fibers, resulting from accumulation of abundant minute grains. This distinctive packing geometry enables the formation of substantially dense

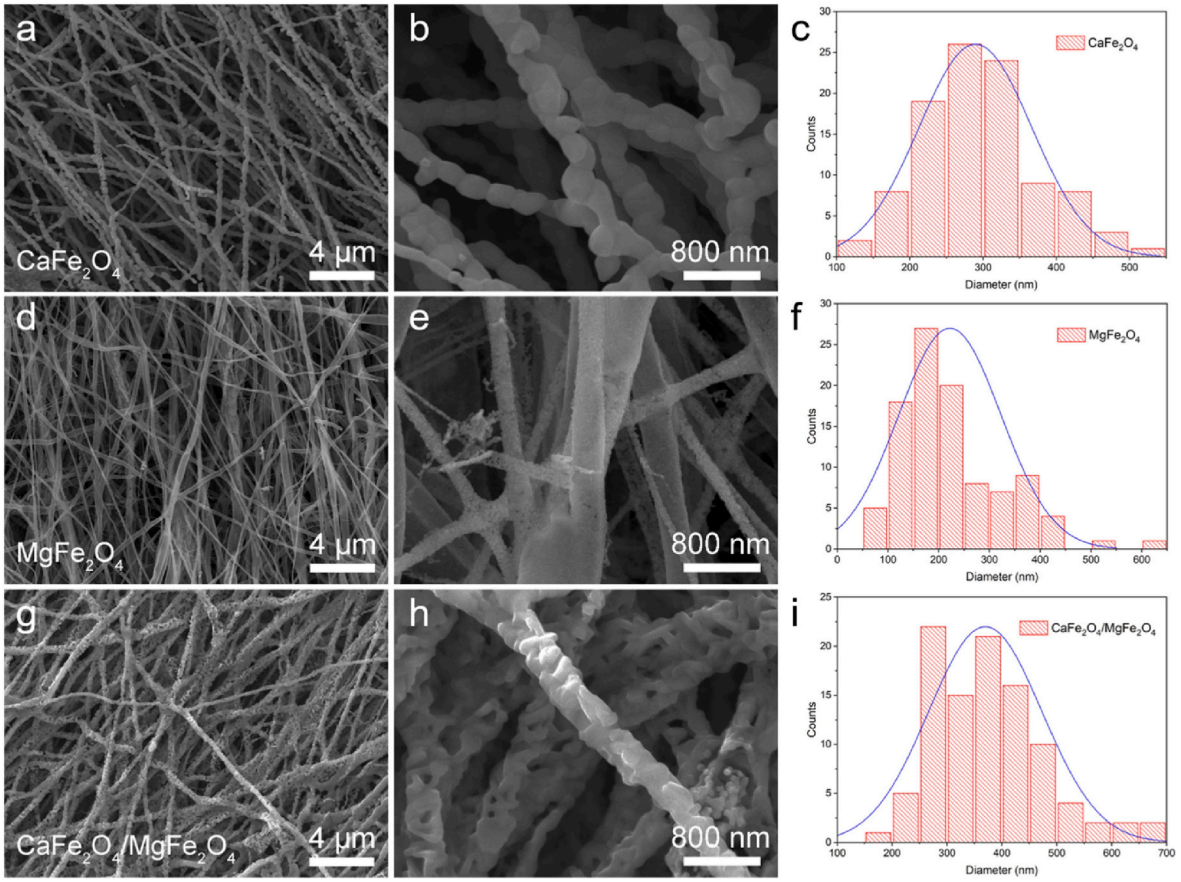


Fig. 1. SEM images and corresponding fiber diameter distributions of $CaFe_2O_4$ (a, b, c), $MgFe_2O_4$ (d, e, f) and $CaFe_2O_4/MgFe_2O_4$ (g, h, i) fibers.

heterointerfaces between $CaFe_2O_4$ and $MgFe_2O_4$ grains [10,39–43].

XPS analysis was carried out to determine the surface chemical states of the $CaFe_2O_4/MgFe_2O_4$ composite fibers (Fig. S2). The Ca 2*p* spectra in Fig. S2a shows two peaks at 350.89 eV and 347.3 eV, which are characteristic of the Ca 2*p* spin-orbit state of Ca^{2+}, confirming the presence of Ca^{2+} in the $CaFe_2O_4/MgFe_2O_4$ fibers [43]. The Mg 1*s* spectra in Fig. S2b show a single peak at 1303.1 eV, corresponding to the Mg 1*s* spin-orbit state of Mg^{2+} [44]. The Fe 2*p* spectra, as shown in Fig. S2c, present characteristic peaks at 724.3 eV and 710.7 eV corresponding to Fe $2p_{1/2}$ and Fe $2p_{3/2}$, indicating the presence of Fe^{3+} [28]. The O 1*s* spectra of $CaFe_2O_4/MgFe_2O_4$ fibers, as shown in Fig. S2d, reveals two types of oxygen environments: lattice oxygen (O^{2-}) at 529.9 eV and surface-adsorbed species at 531.5 eV [10]. These observations collectively validate that the constituent elements exist as Ca^{2+}, Mg^{2+}, Fe^{3+}, and O^{2-}, aligning with the expected ionic states of $CaFe_2O_4$ and $MgFe_2O_4$.

3.2. Microstructural characterization of as-prepared ferrite fibers

To further elucidate the microstructure of the three ferrite fibers and confirm the presence of heterointerfaces in the composite fibers, extensive TEM characterization was carried out. The BF TEM image in Fig. 2a shows that the $CaFe_2O_4$ fibers consist of numerous interconnected crystallites. The corresponding SAED pattern in Fig. $2a_1$ is indexed along the [001] zone-axis of orthorhombic $CaFe_2O_4$, corroborating our XRD results. A representative HRTEM image of an individual nanograin in the $CaFe_2O_4$ fibers is shown in Fig. $2a_2$. The magnified view of the white square area in Fig. $2a_2$ is presented in Fig. $2a_3$. Two sets of lattice fringes with interplanar spacings of 2.67 Å and 2.68 Å are observed, with an included angle of approximately 60°. These lattice fringes can be assigned to the (320) and (040) planes of $CaFe_2O_4$, respectively.

TEM analysis of the $MgFe_2O_4$ fibers is presented in Fig. 2b. The BF image indicates that these fibers are built up from small crystallites. The corresponding SAED pattern in Fig. $2b_1$ exhibits polycrystalline diffraction rings. These rings are indexed as the (111), (220), (311), and (400) planes of cubic $MgFe_2O_4$. Fig. $2b_2$ presents a typical HRTEM image of the $MgFe_2O_4$ fiber, revealing that several nanograins have clear lattice fringes, indicative of good crystallinity. The magnified view in Fig. $2b_3$ resolves two adjacent lattice fringes with interplanar distances of 2.96 Å and 2.53 Å, and an angle of approximately 65°. These two planes are assigned to $(2\,\bar{2}\,0)$ and $(1\bar{1}\,3)$ planes of cubic $MgFe_2O_4$, respectively. For the $CaFe_2O_4/MgFe_2O_4$ composite fibers, the BF image in Fig. 2c shows that the fibers are composed of aggregated particles. Fig. 2d shows the corresponding HRTEM image, clearly revealing that three regions have different lattice fringes. To further investigate their microstructure, the three regions, labeled as grain I, grain II, and interfacial region III in Fig. 2d, were magnified. The corresponding enlarged HRTEM images are displayed in Fig. 2e, f and h, respectively. For grain I in Fig. 2e, lattice spacings of 2.53 Å and an angle of 63° are consistent with the $(\bar{1}\,3\bar{1})$ and $(\bar{3}\,11)$ planes of cubic $MgFe_2O_4$, with the inset of SAED pattern confirming the [112] zone axis. For grain II in Fig. 2f, spacings of 2.67 Å and 2.68 Å, and an angle of 60°, correspond to (320) and (040) planes of $CaFe_2O_4$, as supported by the SAED pattern in Fig. 2g. The HRTEM image of region III, as shown in Fig. 2h, reveals a tightly bonded grain boundary between grains I and II, suggesting the formation of a $CaFe_2O_4/MgFe_2O_4$ heterointerface.

The EDS elemental mapping results, as shown in Fig. S3, provide further evidence that both $CaFe_2O_4$ and $MgFe_2O_4$ coexist within the $CaFe_2O_4/MgFe_2O_4$ composite fibers. Fig. S3a shows a low-magnification TEM image of several nanograins within an individual composite fiber. Fig. S3b is an enlarged image of two overlapped nanograins in Fig. S3a.

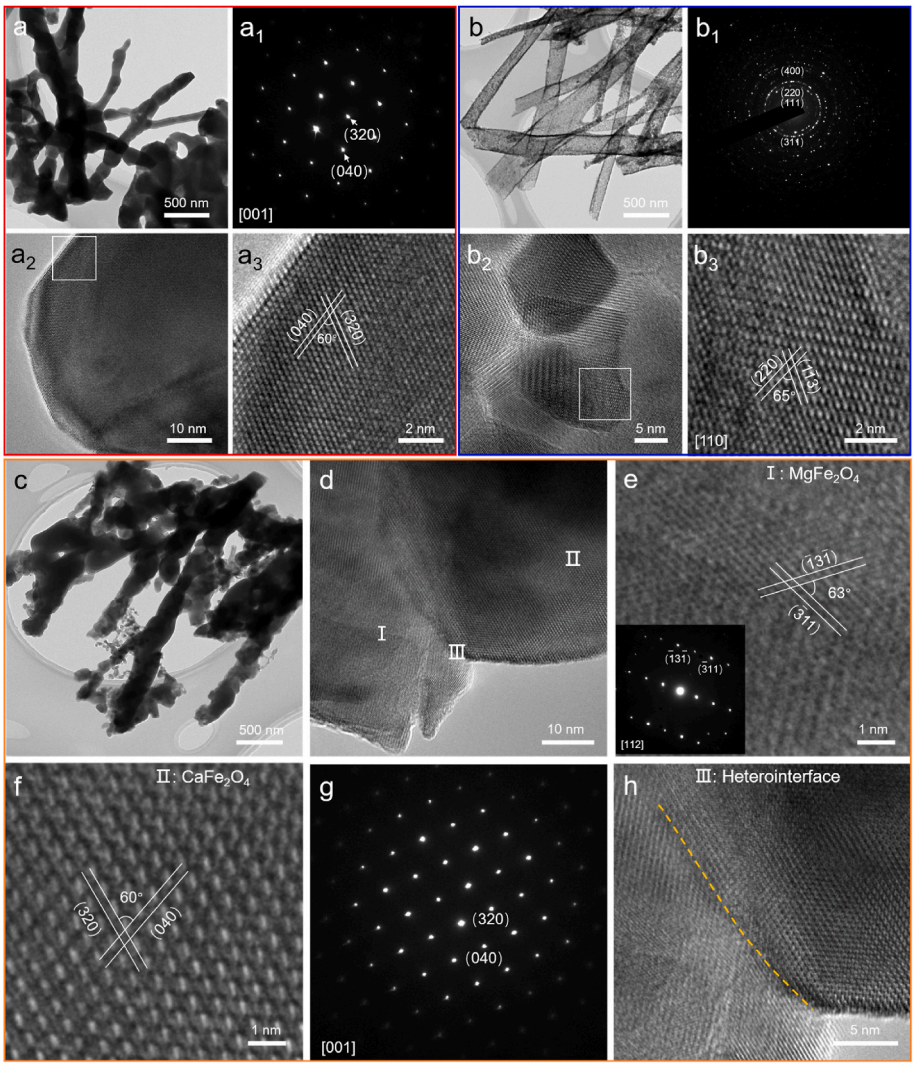


Fig. 2. (a) BF image of $CaFe_2O_4$ submicron fibers, with typical SAED pattern of the grains shown in (a_1), HRTEM image of a single grain in (a_2), and its enlarged view in (a_3); (b) BF image of $MgFe_2O_4$ submicron fibers, with SAED pattern of the fibers in (b_1), HRTEM image of a localized region in (b_2), and its enlarged image in (b_3); (c) BF TEM image of $CaFe_2O_4/MgFe_2O_4$ submicron composite fibers, (d) HRTEM image of nanograins of fiber in (c), (e) HRTEM image of grain I in (d), (f) HRTEM image of grain II in (d), (g) SAED patterns acquired from the grain in (f), (i) Heterointerface between grain I and grain II.

Fig. S3c–f present the EDS elemental mappings of the two nanograins in Fig. S3b. From Fig. S3e and f, we can see that both Fe and O have a uniform spatial distribution within these two grains. In contrast, the elemental mappings of Ca and Mg in Fig. S3c and d display pronounced region-selective distribution, indicating that the two overlapped nanograins are $CaFe_2O_4$ and $MgFe_2O_4$, respectively. These EDS mapping results demonstrate that the $CaFe_2O_4/MgFe_2O_4$ composite fibers contain well-defined $CaFe_2O_4$ and $MgFe_2O_4$ crystallites.

To gain deeper insight into the heterointerface structure between $MgFe_2O_4$ and $CaFe_2O_4$, STEM characterization was performed on the $CaFe_2O_4/MgFe_2O_4$ composite fibers, as presented in Fig. 3. Fig. 3a depicts a typical HAADF image obtained from the interfacial region within the composite fiber. Two crystallites with distinct orientations are clearly visible and labeled as grain I and grain II, and the interfacial region is marked as region III. Detailed lattice analysis of grain I in Fig. 3b identifies the $(3\,\bar{1}\,1)$ and $(22\bar{2})$ reflections of $MgFe_2O_4$, evidenced by measured *d*-spacings of 2.53 Å and 2.42 Å at an intersection angle of 80°. For grain II, the enlarged HAADF image in Fig. 3c exhibits a measured lattice spacing of 5.35 Å, which is assigned to the (020) plane of $CaFe_2O_4$. The enlarged view of the heterointerface in Fig. 3d confirms the intimate atomic contact between $CaFe_2O_4$ and $MgFe_2O_4$. The interface exhibits a well-defined crystallographic orientation relationship: $[001]CaFe_2O_4//[011]MgFe_2O_4$, $(020)CaFe_2O_4//(22\ \bar{2})MgFe_2O_4$. This orientation relationship proves the presence of heterointerfaces in the $CaFe_2O_4/MgFe_2O_4$ composite fibers, which may positively influence their magnetic properties.

3.3. *Magnetic properties of as-prepared ferrite fibers*

The magnetic hysteresis (*M-H*) loops and the corresponding low-field enlargements for the as-prepared fibers are presented in Fig. 4a and b, respectively. Their primary magnetic characteristics are detailed in Table 2. All three ferrite fibers exhibit typical soft-magnetic behavior, characterized by low H_c. Specifically, $MgFe_2O_4$ possesses the smallest H_c of 20 Oe, $CaFe_2O_4$ shows the largest H_c of approximately 70 Oe, and the $CaFe_2O_4/MgFe_2O_4$ composite fibers exhibit an intermediate value of 50 Oe. This suggests that the influence of the heterointerface on H_c remains relatively weak. Although the heterointerface exerts limited influence on H_c of the composite fibers, it has pronounced effect on the magnetization of the composite fibers. Both the M_s and remanent magnetization (M_r) of the composite fibers are significantly higher than those of the single-phase counterparts. The M_s values are 0.19 emu/g for $CaFe_2O_4$, 6.46 emu/g for $MgFe_2O_4$, and 23.60 emu/g for the composite fibers. The M_r values are 0.05 emu/g, 0.39 emu/g, and 2.13 emu/g for

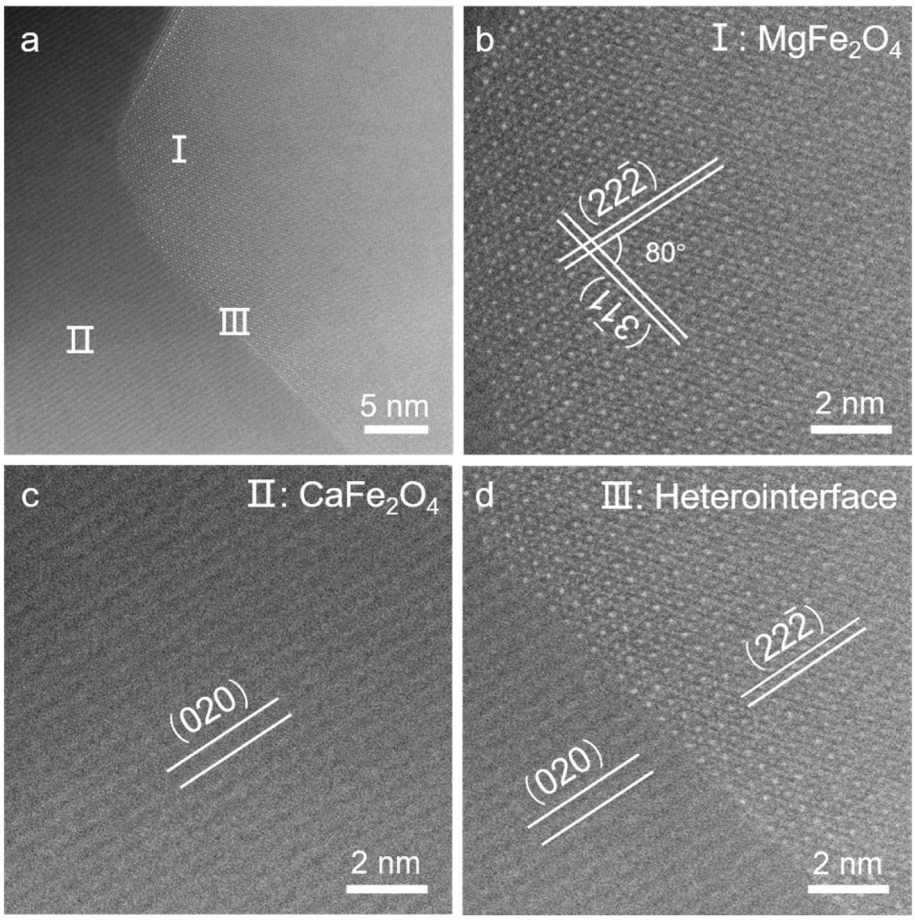


Fig. 3. HAADF images of the $CaFe_2O_4/MgFe_2O_4$ heterostructure interface. (a) Overview of the interface region, (b) Magnified HAADF image of grain I, (c) Enlarged HAADF image of grain II, (d) Close-up views of the interfacial area III.

$CaFe_2O_4$, $MgFe_2O_4$ and the composite fibers, respectively.

The above results clearly demonstrate that heterointerface engineering represents an effective strategy to enhance the magnetization of ferrite materials. Among the three samples, $CaFe_2O_4$ exhibits the highest M_r/M_s ratio, reflecting the strongest magnetization retention capability. Interestingly, introduction of the heterointerfaces in the $CaFe_2O_4/MgFe_2O_4$ composite fibers markedly reduces the M_r/M_s ratio compared to pure $CaFe_2O_4$. It is noteworthy that both H_c and M_s are theoretically linked to the magnetic anisotropy constant (K) according to the well-established relationship given by equ. (1) [45].

$$H_c = \frac{0.96 \times K}{M_s} \quad (1)$$

The effective anisotropy constant (K) was calculated for the three samples, yielding values of 14, 135 and 1229 Oe·emu/g for $CaFe_2O_4$, $MgFe_2O_4$, and the $CaFe_2O_4/MgFe_2O_4$ composite fibers, respectively. Moreover, the composite fibers exhibit a substantially higher K value than the single-phase fibers. This further confirms that heterointerface engineering can significantly enhance the magnetic anisotropy constant of the ferrite fibers.

3.4. Calculations of electronic structure and magnetic moments

To uncover the microscopic origin of the enhanced magnetic performance in composite fibers, we carried out first-principles calculations focusing on the magnetic structures and atomic magnetic moments of Fe in $CaFe_2O_4$, $MgFe_2O_4$, and $CaFe_2O_4/MgFe_2O_4$ heterointerface. First, spin-polarized calculations were performed on the single-phase $CaFe_2O_4$ and $MgFe_2O_4$ to identify the most stable spin configurations, as illustrated in Fig. S4a and b, respectively. Subsequently, a $CaFe_2O_4/MgFe_2O_4$ heterointerface model was constructed based on the optimized single-phase structures, and structural relaxation was carried out to determine the stable interfacial configuration, as shown in Fig. 4c. Based on these models, the *d*-projected and site-projected PDOS, alongside the magnetic moments were computed for Fe atoms in the three systems. For the interface model, we only consider two layers within the blue dashed box in Fig. 4c and select two different types of Fe atoms in each layer to calculate their PDOS and magnetic moments. The PDOS results for Fe atoms at different sites are presented in Fig. 4d.

In the $CaFe_2O_4$ unit cell, as shown in Fig. S4a, Fe atoms occupy two octahedral sites, designated as 4*c*-Fe1 and 4*c*-Fe2 based on their opposing spin orientations. These sites exhibit antiparallel magnetic moments of $-2.547\ \mu_B$ and $+2.677\ \mu_B$, respectively, with a residual net magnetic moment of $0.065\ \mu_B$ per formula unit. For $MgFe_2O_4$, the Fe coordination environment is analogous to that in $CaFe_2O_4$, with Fe atoms occupying octahedral sites with two spin orientations (16*d*-Fe1 and 16*d*-Fe2), as shown in Fig. S4b. The magnetic moments are likewise antiparallel. The PDOS diagram analysis for $MgFe_2O_4$ also reveals a perfect symmetrical distribution of spin up and spin down states for two types of Fe atoms, consistent with the calculated magnetic moments of $-3.063\ \mu_B$ and $+3.063\ \mu_B$ for 16*d*-Fe1 and 16*d*-Fe2, respectively. Consequently, $MgFe_2O_4$ exhibits a net magnetic moment of $0.000\ \mu_B$, characteristic of typical antiferromagnetic behavior.

Compared with the two single-phase systems, the Fe atoms at the $CaFe_2O_4/MgFe_2O_4$ heterointerface exhibit a profound electronic reconstruction. The PDOS in Fig. 4d reveals a substantial depletion of spin-down states for both 4*c*-Fe1 in the $CaFe_2O_4$ layer and 16*d*-Fe1 in the $MgFe_2O_4$ layer within the interface region. This imbalance disrupts the

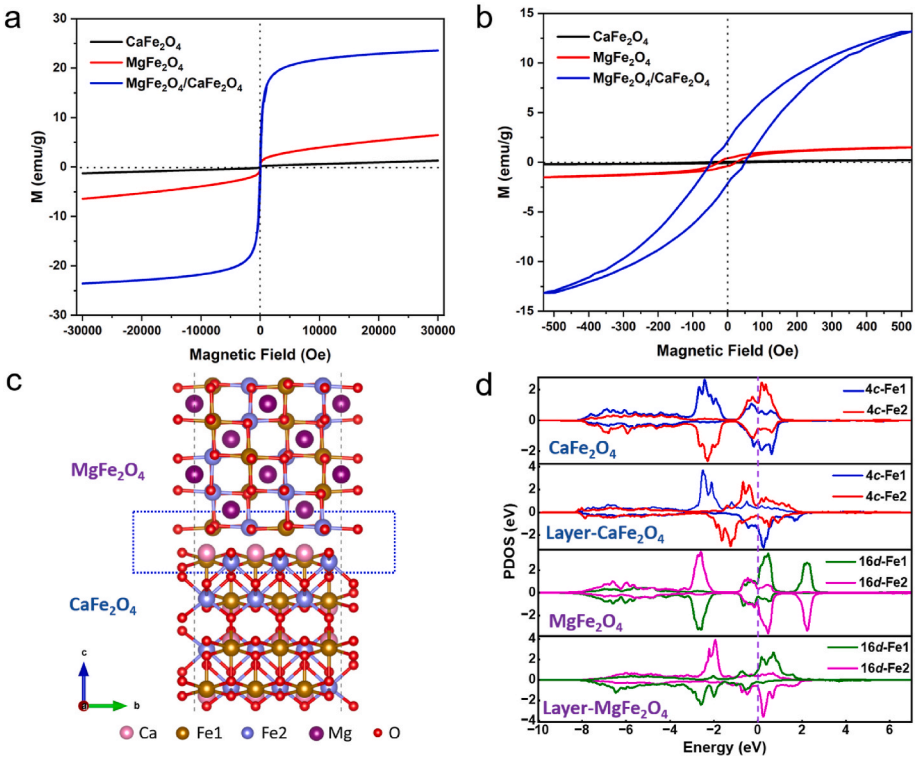


Fig. 4. (a) Room-temperature *M-H* loops of the various ferrite fibers; (b) Enlarged *M-H* curves view in the low-field regime; (c) Structural model of the $CaFe_2O_4$/$MgFe_2O_4$ heterointerface; (d) Calculated Fe PDOS comparing the bulk components with the interface region.

Table 2
Magnetic parameters of $CaFe_2O_4$, $MgFe_2O_4$, and $CaFe_2O_4$/$MgFe_2O_4$ fibers.

Material	H_c (Oe)	M_r (emu/g)	M_s (emu/g)	M_r/M_s	*K* (Oe•emu/g)
$CaFe_2O_4$	70	0.05	0.19	0.26	14
$MgFe_2O_4$	20	0.39	6.46	0.06	135
$CaFe_2O_4$/$MgFe_2O_4$	50	2.13	23.60	0.09	1229

compensation of magnetic moments at the interface region, resulting in a substantially enhanced average net magnetic moment of 0.606 μ_B, far exceeding the values of the single phases. As summarized in Table 3, the calculated magnetic moments confirm that the heterointerface effectively enhances the magnetic performance of the $CaFe_2O_4$/$MgFe_2O_4$ composite, corroborating the experimental observations.

To further explore the source of the enhanced magnetic moment, we performed Bader charge and spin-polarized integrated density of states (IDOS) analyses. According to the Bader charges presented in Table 3, interfacial Fe atoms exhibit noticeable charge redistribution, indicating that electron transfer takes place due to the heterointerface formation. Given that the IDOS near the Fermi level reflects the cumulative electron occupancy, a comparative analysis of spin-projected IDOS provides quantitative insights into the evolution of magnetic moments. The corresponding IDOS curves of Fe *d*-orbital in single phase and heterointerface are presented in Fig. S5.

Table 3
Calculated site-specific Fe magnetic moments for $CaFe_2O_4$, $MgFe_2O_4$, and the $CaFe_2O_4$/$MgFe_2O_4$ heterointerface.

Material	Site	Atom	Bader charge	M (μ_B)	Average M (μ_B)
$CaFe_2O_4$	4*c*	Fe1	1.6875	−2.547	0.065
	4*c*	Fe2	1.6974	2.677	
$MgFe_2O_4$	16*d*	Fe1	1.7698	−3.063	0.000
	16*d*	Fe2	1.7698	3.063	
$CaFe_2O_4$/$MgFe_2O_4$	4*c*	Fe1	1.2765	−1.180	0.606
	4*c*	Fe2	1.5758	2.683	
	16*d*	Fe1	1.6878	−1.362	
	16*d*	Fe2	1.3611	2.283	

For the $CaFe_2O_4$ layer, the Bader charge of the 4*c*-Fe2 atom changes slightly, whereas the 4*c*-Fe1 atom gains a considerable number of electrons after the interface formation. The IDOS results further indicate that these additional electrons mainly occupy the spin-up states, thereby enhancing the local magnetic moment of the 4*c*-Fe1 atom. In the $MgFe_2O_4$ layer, the 16*d*-Fe2 atom shows the most obvious electron gain. The corresponding IDOS curves reveal that the increased electrons predominantly occupy the spin-up states, resulting in a higher local magnetic moment. The above results demonstrate that heterointerface-induced charge redistribution selectively increases the occupation of spin-up states for specific interfacial Fe atoms, serving as the primary mechanism for the improved magnetic performance of the $CaFe_2O_4$/$MgFe_2O_4$ composite.

The experimental results, together with the DFT calculations, suggest that heterointerface engineering plays an important role in improving their magnetic performance. However, the magnetic properties of ferrites can also be influenced by other factors, including grain size, crystal structure, and spin configuration [20,22,46,47]. Further studies are needed to clarify the contributions of interfacial region, grain size, and other microstructural features to the overall magnetic enhancement.

4. Conclusions

In summary, $CaFe_2O_4$ fibers, $MgFe_2O_4$ fibers, and $CaFe_2O_4$/$MgFe_2O_4$ composite fibers were fabricated using electrospinning followed with high-temperature annealing. The $CaFe_2O_4$/$MgFe_2O_4$ composite fibers distinctly improved magnetic properties over the $CaFe_2O_4$ and $MgFe_2O_4$ fibers, demonstrating that heterointerface engineering is effective in boosting the magnetic properties of alkaline-earth metal ferrites. First-principles calculations reveal pronounced reconstruction of the Fe electronic states at the heterointerface between $CaFe_2O_4$ and $MgFe_2O_4$.

In the interfacial region, the spin-down channels of 4*c*-Fe1 sites within the $CaFe_2O_4$ layer and 16*d*-Fe1 sites within the $MgFe_2O_4$ layer are substantially depleted, disrupting the local moment compensation and elevating the average net magnetic moment, far exceeding the values obtained for the single phases. Collectively, this work elucidates a microscopic mechanism whereby the heterointerfaces enhance the magnetic performance of alkaline-earth metal ferrites through the precise regulation of the Fe electronic configurations near the heterointerfaces.

CRediT authorship contribution statement

Zhibin Ling: Writing – original draft, Investigation, Data curation, Conceptualization. **Feiyu Diao:** Writing – review & editing, Supervision, Formal analysis. **Fei Xie:** Resources, Investigation. **Rongsheng Cai:** Validation, Data curation. **Xuyan Xue:** Supervision, Software. **Yiqian Wang:** Writing – review & editing, Supervision, Resources, Funding acquisition, Conceptualization.

Declaration of competing interest

The authors declare that they have no known competing financial interests or personal relationships that could have appeared to influence the work reported in this paper.

Acknowledgments

Financial support from the High-end Foreign Experts Programs of China's Ministry of Science and Technology (Grant Nos. G2022025015L, G2022025016L, H20250033) and the Shandong "Double-Hundred Talent Plan" (Grant No. WST2018006) is gratefully acknowledged. Y. Q. Wang further acknowledges the Taishan Scholar Program of Shandong Province, the Qingdao International Center for Semiconductor Photoelectric Nanomaterials, and the Shandong Provincial University Key Laboratory of Optoelectrical Material Physics and Devices for their additional support.

Appendix ASupplementary data

Supplemental material contains XRD, XPS, TEM-EDS characterizations and first-principles calculation results, including Unit cell of $CaFe_2O_4$ and $MgFe_2O_4$, Fe d-orbital integrated density of states in $CaFe_2O_4$, $MgFe_2O_4$, and $CaFe_2O_4$/$MgFe_2O_4$ heterointerface structure.

Appendix A. Supplementary data

Supplementary data to this article can be found online at https://doi.org/10.1016/j.jpcs.2026.114303.

Data availability

Data will be made available on request.

References

[1] J.M. Silveyra, E. Ferrara, D.L. Huber, T.C. Monson, Soft magnetic materials for a sustainable and electrified world, Science 362 (2018) eaao0195, https://doi.org/10.1126/science.aao0195.
[2] S.X. Wang, N.X. Sun, M. Yamaguchi, S. Yabukami, Properties of a new soft magnetic material, Nature 407 (2000) 150–151, https://doi.org/10.1038/35025142.
[3] G. Herzer, Modern soft magnets: amorphous and nanocrystalline materials, Acta Mater. 61 (2013) 718–734, https://doi.org/10.1016/j.actamat.2012.10.040.
[4] W. Guo, S. Liu, K. Chen, H. Zhang, X. Li, Enhanced sensing performance of the La doped flower-like MoS_2 spheres decorated with $CaFe_2O_4$ nanocube for acetone gas sensor applications, J. Environ. Chem. Eng. 13 (2025) 119890, https://doi.org/10.1016/j.jece.2025.119890.
[5] J. Qu, W. Zhang, Q. Zheng, Y. Xu, L. Xu, B. Cao, Y. Tao, T. Liu, Y. Zhang, N-doped porous hydrochar supported magnesium ferrite for efficiently eliminating lead and tetracycline from the soil environment, J. Environ. Chem. Eng. 14 (2026) 122735, https://doi.org/10.1016/j.jece.2026.122735.
[6] H. Salehi, Z. Javdani, H.A. Badehian, P. Amiri, First-principle study of structural, electronic, and magnetic properties of strontium mono ferrite ceramic, J. Am. Ceram. Soc. 97 (2014) 2832–2841, https://doi.org/10.1111/jace.13016.
[7] M. Ashan, S.A. Alsalhi, A. Kumar, S. Chandra, J. Makasana, S. Ballal, R.S. K. Sharma, P.K. Pathak, R.R. Chaudhary, V. Mishra, Integration of reduced graphene oxide (rGO) into $SrFe_2O_4$ for high-performance supercapacitors, Inorg. Chem. Commun. 174 (2025) 113957, https://doi.org/10.1016/j.inoche.2025.113957.
[8] S.K. Godara, Sneh, V. Kaur, P.S. Malhi, J. Ahmed, S.M. Alshehri, M. Singh, S. Verma, C. Singh, P.K. Maji, P. Kumar, A.M. Tamboli, A.K. Sood, Sol-gel auto-combustion synthesis of double metal-doped barium hexaferrite nanoparticles for permanent magnet applications, J. Solid State Chem. 312 (2022) 123215, https://doi.org/10.1016/j.jssc.2022.123215.
[9] EbtesamE. Ateia, S. Hussien, AmiraT. Mohamed, Tuning the structural and magnetic properties of the stuffed framework structures $MeFe_2O_4$ (Me = Ni, Ca, and Sr), J. Inorg. Organomet. Polym. 33 (2023) 216–227, https://doi.org/10.1007/s10904-022-02497-5.
[10] J. Wang, X. Xue, Y. Wang, Tuning the structural and magnetic properties of electrospun strontium-iron-oxide nanofibers with different stoichiometry, Mater. Charact. 200 (2023) 112884, https://doi.org/10.1016/j.matchar.2023.112884.
[11] A. Manohar, V. Vijayakanth, N. Mameda, K. Sivajee Ganesh, K. Hyeon Kim, Revolutionizing nanoscience: exploring the multifaceted applications and cutting-edge advancements in spinel $CaFe_2O_4$ nanoparticles – a review, Inorg. Chem. Commun. 161 (2024) 111999, https://doi.org/10.1016/j.inoche.2023.111999.
[12] H.H. Shareef, H. Sadiq, H. Sadiq, M. Kanwal, Enhanced specific absorption rate in $MgFe_2O_4$/Graphene nanoplatelets nanocomposites for efficient magnetic hyperthermia therapy, Solid State Sci. 179 (2026) 108400, https://doi.org/10.1016/j.solidstatesciences.2026.108400.
[13] W. Li, Y. Pu, Y. Ying, Y. Kang, J. Yu, J. Zheng, L. Qiao, J. Li, S. Che, Magnetic properties and related mechanisms of iron-based soft magnetic composites with high thermal stability *in situ* composite-ferrite coating, J. Alloys Compd. 829 (2020) 154533, https://doi.org/10.1016/j.jallcom.2020.154533.
[14] W. Li, W. Wang, J. Lv, Y. Ying, J. Yu, J. Zheng, L. Qiao, S. Che, Structure and magnetic properties of iron-based soft magnetic composite with Ni-Cu-Zn ferrite–silicone insulation coating, J. Magn. Magn Mater. 456 (2018) 333–340, https://doi.org/10.1016/j.jmmm.2018.02.033.
[15] Z. Birčáková, J. Füzer, P. Kollár, M. Streckova, J. Szabó, R. Bureš, M. Fáberová, Magnetic properties of Fe-based soft magnetic composite with insulation coating by resin bonded Ni-Zn ferrite nanofibres, J. Magn. Magn Mater. 485 (2019) 1–7, https://doi.org/10.1016/j.jmmm.2019.04.060.
[16] K.J. Sunday, M.L. Taheri, NiZnCu-ferrite coated iron powder for soft magnetic composite applications, J. Magn. Magn Mater. 463 (2018) 1–6, https://doi.org/10.1016/j.jmmm.2018.05.030.
[17] M. Yan, S. Yi, X. Fan, Z. Zhang, J. Jin, G. Bai, High-frequency MnZn soft magnetic ferrite by engineering grain boundaries with multiple-ion doping, J. Mater. Sci. Technol. 79 (2021) 165–170, https://doi.org/10.1016/j.jmst.2020.12.009.
[18] Y. Peng, Y. Yi, L. Li, H. Ai, X. Wang, L. Chen, Fe-based soft magnetic composites coated with NiZn ferrite prepared by a co-precipitation method, J. Magn. Magn Mater. 428 (2017) 148–153, https://doi.org/10.1016/j.jmmm.2016.12.024.
[19] S. Damerio, A.A. Kaverzin, V. Ocelík, G.R. Hoogeboom, B.J. Van Wees, B. Noheda, Antiferromagnetic ordering and uncoupled spins in $CaFe_2O_4$ thin films probed by spin hall magnetoresistance, Adv. Electron. Mater. 8 (2022) 2100963, https://doi.org/10.1002/aelm.202100963.
[20] A.K. Das, R. Govindaraj, A. Srinivasan, Structural and magnetic properties of sol-gel derived $CaFe_2O_4$ nanoparticles, J. Magn. Magn Mater. 451 (2018) 526–531, https://doi.org/10.1016/j.jmmm.2017.11.102.
[21] A. Anagha, A. Joshua, B. Chacko, T. Avanish Babu, S. Srigiri, W. Madhuri, Structural, optical and magnetic properties of $MgFe_2O_4$ and $Ni_{0.5}Zn_{0.5}Fe_2O_4$, Mater. Chem. Phys. 313 (2024) 128746, https://doi.org/10.1016/j.matchemphys.2023.128746.
[22] B. Aslibeiki, G. Varvaro, D. Peddis, P. Kameli, Particle size, spin wave and surface effects on magnetic properties of $MgFe_2O_4$ nanoparticles, J. Magn. Magn Mater. 422 (2017) 7–12, https://doi.org/10.1016/j.jmmm.2016.08.057.
[23] I. Khishigdemberel, E. Uyanga, H. Hirazawa, D. Sangaa, Influence of Cu dope on the structural behavior of $MgFe_2O_4$ at various temperatures, Phys. B Condens. Matter 544 (2018) 73–78, https://doi.org/10.1016/j.physb.2018.05.032.
[24] B.C. Manjunatha, S.A. Sattar, J. Kavana, P. Shankar, H.S. Yoganand, G.V. Ashok Reddy, K. Naveen Kumar, N. Pushpa, Nickel-doped calcium nano ferrites suitable for magneto-electronic applications, Phys. B Condens. Matter 726 (2026) 418207, https://doi.org/10.1016/j.physb.2025.418207.
[25] Y.-H. Chang, W.-C. Tseng, C.-C. Kaun, Y.-H. Su, J.-J. Wu, $Mg_2Fe_2O_5$ nanoparticle-decorated $Ca_2Fe_2O_5$-$CaFe_2O_4$ heterostructure for efficient photocatalytic CO_2 conversion, ACS Sustainable Chem. Eng. 10 (2022) 12651–12658, https://doi.org/10.1021/acssuschemeng.2c03378.
[26] Y. Zu, Y. Zhao, K. Xu, Y. Tong, F. Zhao, Preparation and comparison of catalytic performance for nano $MgFe_2O_4$, GO-loaded $MgFe_2O_4$ and GO-coated $MgFe_2O_4$ nanocomposites, Ceram. Int. 42 (2016) 18844–18850, https://doi.org/10.1016/j.ceramint.2016.09.030.
[27] P. Heidari, S.M. Masoudpanah, A facial synthesis of $MgFe_2O_4$/RGO nanocomposite powders as a high performance microwave absorber, J. Alloys Compd. 834 (2020) 155166, https://doi.org/10.1016/j.jallcom.2020.155166.
[28] W. Guo, L. Huang, X. Liu, J. Wang, J. Zhang, Enhanced isoprene gas sensing performance based on p-$CaFe_2O_4$/n-$ZnFe_2O_4$ heterojunction composites, Sensor.

Actuator. B Chem. 354 (2022) 131243, https://doi.org/10.1016/j.snb.2021.131243.
[29] H.G. Kim, P.H. Borse, J.S. Jang, E.D. Jeong, O.-S. Jung, Y.J. Suh, J.S. Lee, Fabrication of $CaFe_2O_4/MgFe_2O_4$ bulk heterojunction for enhanced visible light photocatalysis, Chem. Commun. (2009) 5889, https://doi.org/10.1039/b911805e.
[30] L. Liang, W. Gu, Y. Wu, B. Zhang, G. Wang, Y. Yang, G. Ji, Heterointerface engineering in electromagnetic absorbers: new insights and opportunities, Adv. Mater. 34 (2022) 2106195, https://doi.org/10.1002/adma.202106195.
[31] H. Kwon, Y. Yang, G. Kim, D. Gim, M. Ha, Anisotropy in magnetic materials for sensors and actuators in soft robotic systems, Nanoscale 16 (2024) 6778–6819, https://doi.org/10.1039/D3NR05737B.
[32] M.W. Van De Putte, D. Polishchuk, N. Gauquelin, J. Verbeeck, G. Koster, M. Huijben, Control of magnetic shape anisotropy by nanopillar dimensionality in vertically aligned nanocomposites, ACS Appl. Electron. Mater. 6 (2024) 3695–3703, https://doi.org/10.1021/acsaelm.4c00371.
[33] C. Zhang, J. Pang, G. Dong, S. Zhang, Q. Wu, Y. Shi, Y. Wang, Single-crystal growth and magnetic properties of quasi-one-dimensional Ce_3MnBi_5, Phys. Rev. Mater. 9 (2025) 054404, https://doi.org/10.1103/PhysRevMaterials.9.054404.
[34] F. Xie, M. Sun, X. Sheng, Q. Zhang, Z. Ling, S. Hao, F. Diao, Y. Wang, Graphene-wrapped Fe_2TiO_5 nanoparticles with enhanced performance as lithium-ion battery anode, Mater. Lett. 358 (2024) 135877, https://doi.org/10.1016/j.matlet.2024.135877.
[35] F. Xie, X. Sheng, Z. Ling, S. Hao, Q. Zhang, M. Sun, G. Liu, F. Diao, Y. Wang, Flexible electrospun iron/manganese-based compounds/carbon fibers: phase transformation and electrochemical properties, Electrochim. Acta 470 (2023) 143288, https://doi.org/10.1016/j.electacta.2023.143288.
[36] X. Sheng, T. Li, M. Sun, G. Liu, Q. Zhang, Z. Ling, S. Gao, F. Diao, J. Zhang, F. Rosei, Y. Wang, Flexible electrospun iron compounds/carbon fibers: phase transformation and electrochemical properties, Electrochim. Acta 407 (2022) 139892, https://doi.org/10.1016/j.electacta.2022.139892.
[37] G. Kresse, J. Furthmüller, Efficient iterative schemes for *ab initio* total-energy calculations using a plane-wave basis set, Phys. Rev. B 54 (1996) 11169–11186, https://doi.org/10.1103/PhysRevB.54.11169.
[38] L. Zhang, F. Xie, S. Hao, F. Diao, Y. Wang, Annealing condition engineering of electrospun iron-titanium oxide nanofibers for enhanced lithium storage performance, Electrochim. Acta 536 (2025) 146746, https://doi.org/10.1016/j.electacta.2025.146746.
[39] S. Hao, B. Zhang, Q. Zhang, M. Sun, R. Cai, F. Diao, Y. Wang, Effectiveness of three distinct strategies of constructing ZnO-based composites for enhanced electrochemical performance, J. Phys. Chem. Solid. 211 (2026) 113502, https://doi.org/10.1016/j.jpcs.2025.113502.
[40] M. Sun, G. Liu, S. Hao, F. Diao, F. Rosei, R. Cai, Y. Wang, Correlation between spinel structure and electrochemical kinetic behavior of spinel ferrites, J. Electroanal. Chem. 1005 (2026) 119870, https://doi.org/10.1016/j.jelechem.2026.119870.
[41] B. Zhang, F. Xie, S. Hao, M. Sun, F. Diao, R. Cai, Y. Wang, Effect of annealing atmosphere on the phase composition and electrochemical properties of iron-oxide-based electrospun nanofibers, J. Energy Storage 124 (2025) 116851, https://doi.org/10.1016/j.est.2025.116851.
[42] J. Wang, X. Sheng, S. Hao, G. Liu, R. Cai, X. Xue, Y. Wang, Construction of $Fe_{0.64}Ni_{0.36}$@graphite nanoparticles via corrosion-like transformation from $NiFe_2O_4$ and surface graphitization in flexible carbon nanofibers to achieve strong wideband microwave absorption, J. Colloid Interface Sci. 657 (2024) 193–207, https://doi.org/10.1016/j.jcis.2023.11.145.
[43] Z. Ling, F. Diao, F. Xie, R. Cai, X. Xue, Y. Wang, Heterointerface-induced enhancement of magnetization in $CaFe_2O_4/Ca_2Fe_2O_5$ composite fibers, Mater. Charact. 238 (2026) 116669, https://doi.org/10.1016/j.matchar.2026.116669.
[44] W. Fan, M. Li, H. Bai, D. Xu, C. Chen, C. Li, Y. Ge, W. Shi, Fabrication of $MgFe_2O_4/MoS_2$ heterostructure nanowires for photoelectrochemical catalysis, Langmuir 32 (2016) 1629–1636, https://doi.org/10.1021/acs.langmuir.5b03887.
[45] R. Sharma, S. Singhal, Structural, magnetic and electrical properties of zinc doped nickel ferrite and their application in photo catalytic degradation of methylene blue, Phys. B Condens. Matter 414 (2013) 83–90, https://doi.org/10.1016/j.physb.2013.01.015.
[46] A.I. Zhernovoi, A.A. Komlev, S.V. D'yachenko, Magnetic characteristics of $MgFe_2O_4$ nanoparticles obtained by glycine–nitrate synthesis, Tech. Phys. 61 (2016) 302–305, https://doi.org/10.1134/S1063784216020274.
[47] S. Maensiri, M. Sangmanee, A. Wiengmoon, Magnesium ferrite ($MgFe_2O_4$) nanostructures fabricated by electrospinning, Nanoscale Res. Lett. 4 (2009) 221, https://doi.org/10.1007/s11671-008-9229-y.